Geophysical Journal International

Geophys. J. Int. (2014) doi: 10.1093/gji/ggu031

Geophysical Journal International Advance Access published February 21, 2014

Strong seismic wave scattering in the low-velocity anomaly associated with subduction of oceanic plate

Shunsuke Takemura and Kazuo Yoshimoto

Graduate School of Nanobioscience, Department of Materials System Science, Yokohama City University, 22-2 *Seto, Kanazawa, Yokohama* 236-0027*, Japan.*
E-mail: shunsuke@yokohama-cu.ac.jp

Accepted 2014 January 24. Received 2014 January 23; in original form 2013 October 29

SUMMARY

Analyses of dense seismic records in Kanto, Japan, revealed distinct pulse broadening and peak delay of high-frequency *S* waves at central Chiba. These phenomena are observed at frequency range of 1–8 Hz and exist only for ray paths passing through the low-velocity (LV) zone at depth of 20–40 km beneath northwestern Chiba. To obtain a more detailed understanding of these phenomena, we conducted 2-D and 3-D finite difference method simulations of seismic wave propagation using a realistic heterogeneous structure model. Through numerous simulations we demonstrated that strong seismic scattering, due to localized strong small-scale heterogeneities in the LV zone and in the oceanic crust, is a major cause of strong pulse broadening and peak delay of high-frequency *S* waves. After comparing simulation results with observations, the most preferable small-scale velocity heterogeneity in the LV zone is characterized by a Gaussian power spectral density function (PSDF) with correlation distance a of 1–2 km and rms value $\varepsilon = 0.07$–0.09, superposed on a background exponential PSDF ($a = 3$ km, $\varepsilon = 0.07$). Assuming strong velocity heterogeneities, observed amplitude decay at Chiba is also well explained by strong scattering attenuation in the LV zone. Because the LV zone, which has been reported by seismic tomography studies, is interpreted as being constructed by the dehydration of the subducting oceanic crust of the Philippine Sea Plate, strong small-scale velocity heterogeneity in the LV zone may be related to the random distribution of fluid in this volume.

Key words: Body waves; Seismic attenuation; Computational seismology; Wave scattering and diffraction; Wave propagation.

GJI Seismology

1 INTRODUCTION

The propagation features of high-frequency (>1 Hz) seismic waves are strongly affected by scattering and diffraction due to the heterogeneous structures in the lithosphere. Many studies have reported that *S* waves of local and/or regional earthquakes show pulse broadening and peak delay (defined as the lag time from onset to peak amplitude arrival) with increasing propagation distance (e.g. Sato 1989; Obara & Sato 1995). The results of these studies revealed the existence of small-scale velocity heterogeneities along propagation paths, even at depths of more than several tens of kilometres.

Saito *et al.* (2005) analysed pulse broadening and maximum amplitude decay of *S* waves as a function of hypocentral distance at the eastern side of northeastern Japan, and estimated the heterogeneous velocity structure based on the Markov approximation in a randomly homogeneous distribution of small-scale velocity heterogeneities. Discarding unrealistic assumption of a spatially uniform heterogeneity, Takahashi *et al.* (2007, 2009) determined the 3-D heterogeneous structure by analysing the propagation-path dependence of *S*-wave peak delay, relating it to strong small-scale velocity heterogeneity in Quaternary volcanoes in the northeastern Japan.

The studies described above did not consider large-scale 3-D heterogeneous structures, such as the crust, mantle and subducted oceanic plate, because of the difficulty in including these features in theoretical models. However, pulse broadening of *S* waves is likely to occur even in such structures. Many studies have reported the trapping of seismic waves by continental or oceanic crusts (e.g. Hori *et al.* 1985; Fukao *et al.* 1983; Kennett & Furumura 2001, 2008), which are relatively low-velocity (LV) regions compared with the surrounding structures. Furumura & Kennett (2005) and Kennett & Furumura (2008) revealed that high-frequency waves are trapped effectively by multiple forward scattering due to the non-isotropic small-scale velocity heterogeneities in the subducted oceanic plate.

In the Kanto region of Japan (Fig. 1a), the seismic velocity structure is complicated by the presence of two subducted oceanic plates (i.e. the Pacific and Philippine Sea plates) and a sedimentary basin

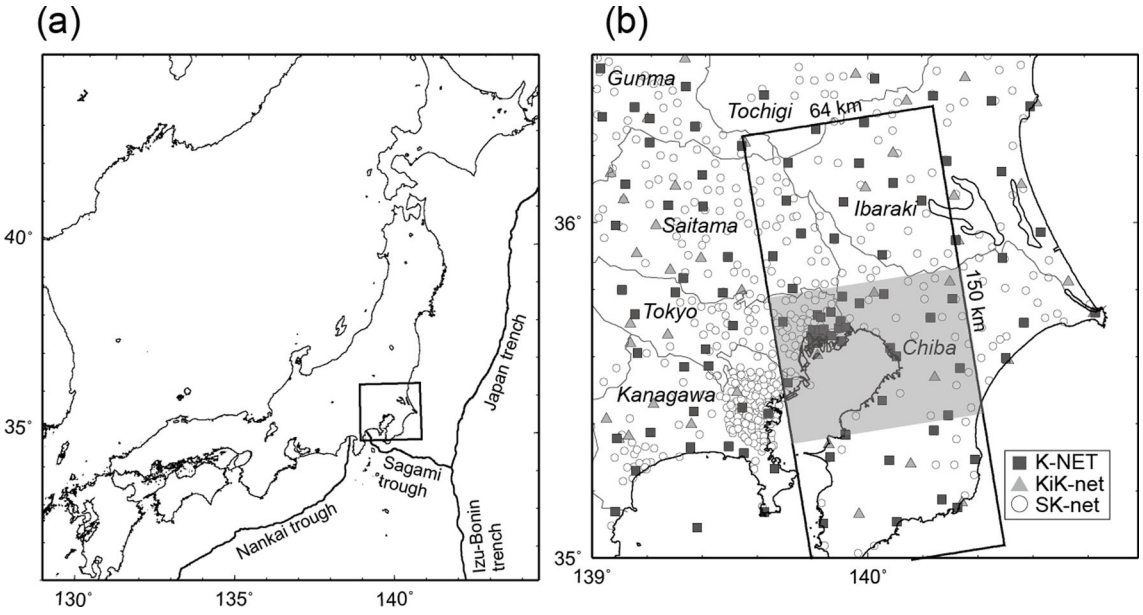

Figure 1. (a) Study area in Japan, and (b) the distribution of seismic stations of K-NET/KiK-net and SK-net in the Kanto region. The region inside the rectangle in (b) is the area of 3-D FDM simulation, and the shaded area represents the assumed LV zone in 3-D simulation.

(i.e. the Kanto basin). Many researchers have investigated the heterogeneous velocity structures in and around the Kanto region in order to understand the relationship between seismic wave propagation and heterogeneous structure and to contribute to disaster mitigation associated with future large earthquakes (e.g. Matsubara *et al.* 2005, 2008; Koketsu *et al.* 2008). However, the detailed 3-D heterogeneous structure of this region still remains uncertain, especially for small-scale velocity heterogeneities that strongly affect high-frequency seismic wave propagation.

To understand propagation features of seismic waves in the complex Kanto region, we analysed pulse broadening and peak delay of high-frequency *S* waves derived from a large number of seismograms recorded by dense strong motion arrays. To examine the relationship between the observed pulse broadening of high-frequency *S* waves in the Kanto region and the heterogeneous subsurface structure, we conducted 2-D and 3-D finite difference method (FDM) simulations of seismic wave propagation. Using FDM simulations, we are able to examine the effects of large-scale heterogeneous structures as well as small-scale velocity heterogeneities on high-frequency seismic wave propagation. We demonstrated that a localized heterogeneous anomaly beneath this region is major cause of the distinct pulse broadening and peak delay of *S* waves observed at central Chiba. By comparing simulation results with observations from dense seismic networks in the Kanto region, we also estimated the statistical characteristics of the small-scale heterogeneity in this anomaly.

2 OBSERVED FEATURES OF HIGH-FREQUENCY SEISMIC WAVES IN THE KANTO REGION

To investigate characteristics of seismic wave propagation in the Kanto region, we used data from dense strong motion networks (K-NET/KiK-net) operated by the National Research Institute for Earth Science and Disaster Prevention (NIED) of Japan. To achieve denser waveform analysis, we also used data from intensity metres (SK-net) located at city government offices, fire stations and other sites in the Kanto region. At each station of both strong motion and intensity metre networks, a trigger-type three-component accelerometer is installed on the free surface. The integrated seismic network of strong motion seismometers and intensity metres is shown in Fig. 1(b).

Using dense seismic networks, we obtained detailed characteristics of seismic wave propagation through heterogeneous structures beneath the Kanto region. For example, velocity waveforms of radial (R) and transverse (T) components during an event, which occurred at a depth of 53 km beneath the southern Ibaraki on 2005 October 16 are shown in Fig. 2.

It has been well recognized that seismic waves in the sedimentary basin are strongly amplified by thick LV sediments (Fig. 2e). Waveforms recorded in the basin area (Figs 2b–d) showed much larger amplitudes and longer durations of *S* waves compared with those in the mountain area (TKY001; Fig. 2a). However, a careful observation of this figure reveals clear differences in the waveforms of *S* waves recorded in the basin area, even though there was not a significant difference in local sediment thickness. In particular, waveforms recorded at central Chiba (CHB014; Fig. 2d) showed gradual onset and spindle shape of *S* wave. In addition, peak arrival time of *S* waves was much delayed compared with those at other stations. Such strong peak delay and spindle shape of *S* wave might be strongly related to heterogeneous velocity structures along the propagation paths (e.g. Saito *et al.* 2005; Takahashi *et al.* 2007) or to local site or sedimentary structures just below the seismic station (e.g. Koketsu & Miyake 2008).

To examine frequency change property of spindle-shape seismograms, we applied a set of bandpass filters with a passed band frequencies of $f = 0.25$–0.5, 0.5–1, 1–2, 2–4, 4–8 and 8–16 Hz, to velocity seismogram of R component recorded at station CHB014 (Fig. 3). Because of the relatively deep hypocentre depth (53 km), surface waves do not appear clearly, and direct *S* waves are therefore dominant for all frequency bands. At low frequencies (0.25–0.5, 0.5–1 Hz), clear *S*-wave pulses were observed, durations of *S* waves were less than 10 s and peak amplitudes appear close to the

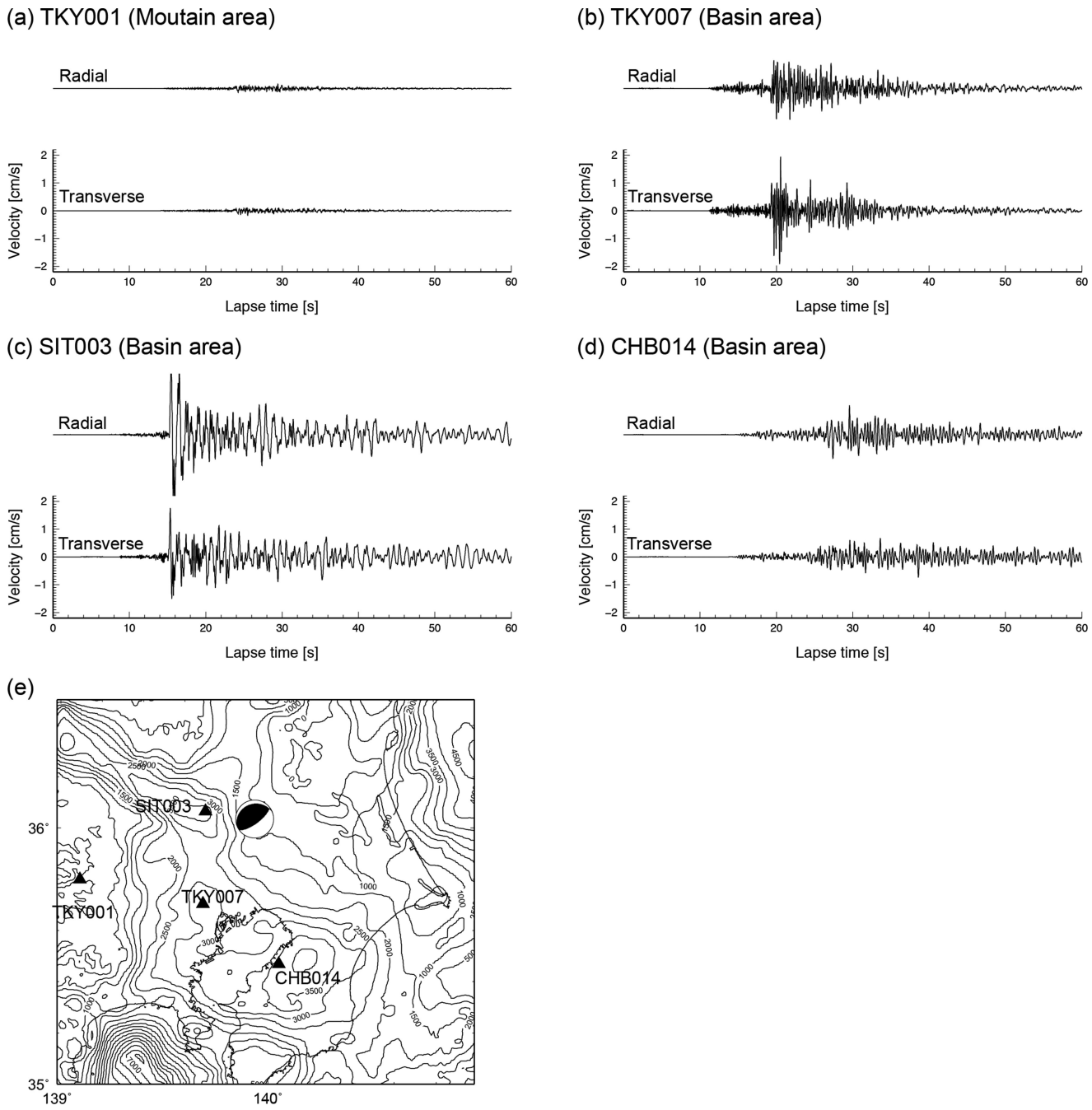

Figure 2. Velocity waveforms of radial and transverse components recorded at stations (a–d) in the Kanto region, Japan, during M_w 5.0 earthquake that occurred at a depth of 53 km beneath southern Ibaraki on 2005 October 16. Locations of stations and epicentre are shown in (e). Contour lines in (e) represent the basement depth (m) proposed by Koketsu *et al.* (2008).

onset of *S* waves. As frequency increases over 1 Hz, duration of *S* waves broadens to become larger than 10 s. At higher frequencies (2–4, 4–8 Hz), onset of *S* waves became unclear, and peak arrival is strongly delayed. Using filtered seismograms, we confirmed that strong peak delay and spindle shape of *S* waves appeared clearly at higher frequencies (>1 Hz). Thus, we focused our analyses on the characteristics of high-frequency (>1 Hz) seismic wave propagation in the Kanto region.

In order to show how spindle-shape *S* waves at central part of Chiba develop during propagation, Fig. 4 shows *R* component velocity seismograms aligned from the epicentre in different directions towards Chiba, eastern Kanagawa and western Tokyo (stations are plotted in Fig. 4d). Almost all stations are located at thick sediment area. A bandpass filter with frequency of 2–4 Hz was applied to each seismogram, and each trace was normalized by its maximum amplitude to examine the envelope shape of *S* waves. As shown in Fig. 4, waveforms showed different features in each direction, even though there was not a significant difference in basement depth. The strong peak delay and broadening of *S* waves were not apparent in the direction to Chiba at shorter epicentral distances ($D < 30$ km; Fig. 4a), and clear *S*-wave pulses were observed. As distance increased to around 30–40 km, an anomalous sudden change in onset, strong peak delay and broadening of *S* waves appeared. At larger distances (>50 km), waveforms were showing spindle shapes with

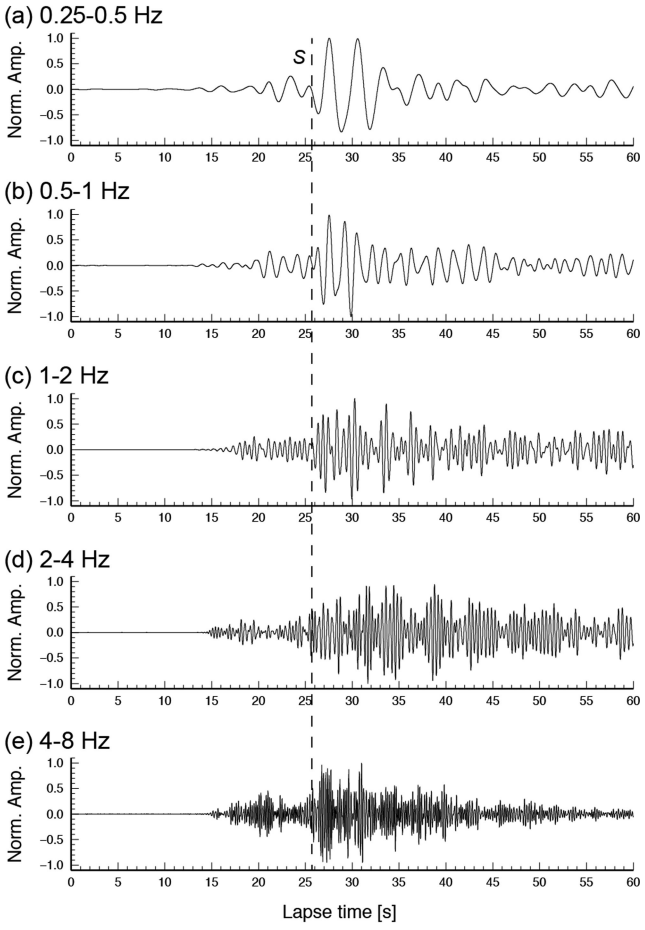

Figure 3. Filtered radial component seismogram recorded at station CHB014 (see Fig. 2d) during M_w 5.0 earthquake that occurred at a depth of 53 km beneath southern Ibaraki on 2005 October 16. Each trace was normalized by its maximum amplitude. Passed band frequencies of filter were (a) 0.25–0.5, (b) 0.5–1, (c) 1–2, (d) 2–4 and (e) 4–8 Hz, respectively. The dashed line indicates onset of direct *S* wave.

strong peak delay. However, in the direction towards the eastern side of Kanagawa (Fig. 4b), broadening and peak delay of *S* waves increased with increasing distance, but sudden changes and spindle-shape *S* waves did not appear. We also found a similar tendency in pulse broadening of *S* waves in the direction towards the southwestern part of Tokyo (Fig. 4c). At southwestern part of Tokyo, however, seismic stations are not densely distributed, and a sudden change in pulse broadening and peak delay was not clear at this region compared with those at Chiba. Thus, we focused our study on the characteristics of high-frequency seismic wave propagation in the direction of Chiba.

Fig. 5 shows the spatial distribution and distance change of peak arrival times of velocity seismograms for frequency of 2–4 Hz. The values of peak amplitude and arrival time were measured from the sum of rms envelopes of two horizontal components. If seismic waves propagate in a homogeneous medium, peak arrival time simply increases depending on hypocentral distance from the seismic source. Therefore, in the case of a homogenous medium, the spatial distribution of peak arrival time should show an isotropic or concentric pattern. However, observed spatial distribution (Fig. 5a) was not showing clear concentric pattern. Especially, peak arrival time at Chiba suddenly increases from 20 to 30 s. We also show peak arrival time of velocity seismograms for frequency of 2–4 Hz as a function of hypocentral distance in Fig. 5(b); a sudden change in peak arrival times at hypocentral distance of 60–70 km appeared at Chiba, but similar patterns were not observed for other regions. However, peak arrival time data derived from a single event were widely scattered, and such a small data set was not enough to obtain average characteristics of distance change in peak arrival time for Chiba and other regions of Kanto.

To understand average characteristics of distance changes in peak arrival times and their frequency dependence property, we examined distance changes in peak arrival times for different frequency bands. Fig. 6 shows moving average curves and observed peak arrival time data for different frequency bands (1–2, 2–4, 4–8 and 8–16 Hz) as a function of hypocentral distance. Peak arrival times were measured using 1779 strong motion records during 10 earthquakes with similar mechanisms and hypocentre locations (see Table 1 and upper right part of Fig. 6b). To obtain moving average curve of peak arrival time as a function of hypocentral distance, we first divided the data based on hypocentral distance into 5 km intervals with an overlap of 2.5 km and then calculated average values of peak arrival time at each distance. Obtained moving average curves show averaged path effect from the source region to the receiver at each distance.

Because peak arrival time data for each frequency band were very scattered, it was suspected that abnormally large and small peak arrival times might cause a shift in the averaged values. To check this possibility, we also plotted histogram of peak arrival times for frequency of 2–4 Hz at distance of 80–120 km (Fig. 7). It is clear that distribution of peak arrival times in the Kanto region (grey bars) was asymmetric, but almost all peak arrival times were occurring at times of 20–30 s, which are close to theoretical *S*-wave arrival times at distances of 80–120 km. In contrast, peak arrival times at Chiba (black bars) were larger, and almost all the data were appearing at times of 30–40 s. In histograms, abnormally large and small values of peak arrival times were not so much, indicating that the effect of shift in the average values might be negligible in our averaging procedure.

At frequencies of 1–2 and 2–4 Hz (Figs 6a and b), there were sudden delays in the average peak arrival times at Chiba at hypocentral distances larger than 60–70 km. At a hypocentral distance of about 100 km, peak arrival was delayed by about 10 s compared to other regions. As frequency increased, the gap between Chiba and other regions became smaller, and, at higher frequencies (i.e. 8–16 Hz; Fig. 6d), we did not observe significant peak delays. Strong peak delays of *S* waves at Chiba were dominant at frequency range of 1–8 Hz.

According to the above analysis, observed seismograms at Chiba were clearly distorted. They revealed unclear onset and strong peak delays for *S* waves propagating beneath the northwestern part of Chiba, where the LV zone with relatively high V_P/V_S ratio of 1.80–1.90 above the oceanic crust of the Philippine Sea Plate (e.g. Kamiya & Kobayashi 2000; Matsubara *et al.* 2005, 2008), and the strong low-Q zone coincided with this LV zone (e.g. Nakamura *et al.* 2006; Furumura & Takeuchi 2007) exist.

Fig. 8 shows filtered velocity seismograms of *R* component for frequency of 2–4 Hz recorded for the events (with various depths and locations) by three K-NET stations. The list of events is shown in Table 2, and distribution of epicentres and stations is shown in Fig. 8(d). The LV zone at depth of 20–40 km estimated by tomography studies is shown in the shaded area of the map. Seismograms recorded at IBR010 (Fig. 8a) showed clear *S*-wave onset, except in event C, which occurred at depth of 89 km beneath southern Chiba. Large amplitude coda waves associated with sedimentary

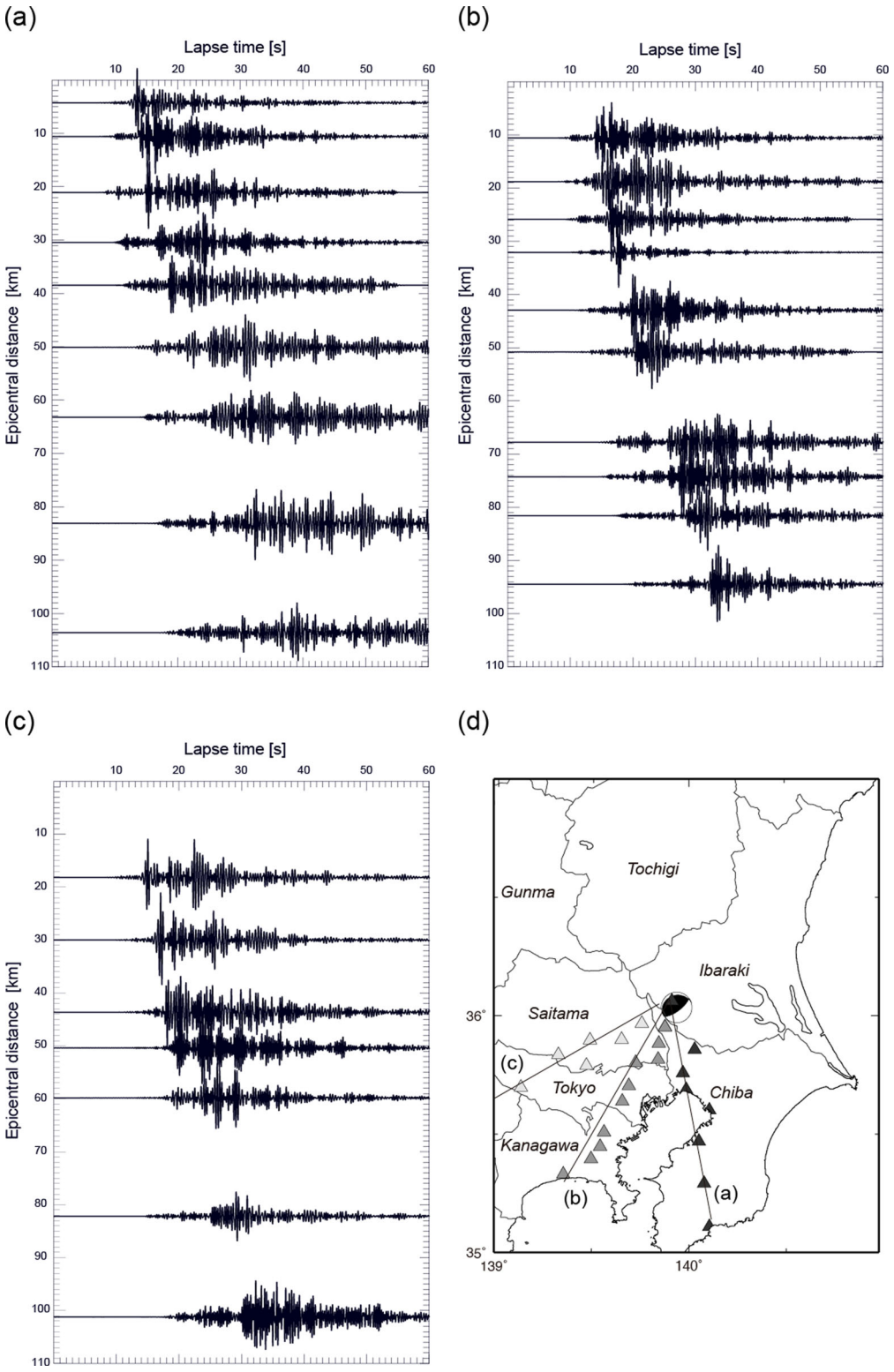

Figure 4. Filtered waveforms of radial component ground velocity motion for the M_w 5.0 earthquake that occurred at a depth of 53 km beneath southern Ibaraki on 2005 October 16. Waveforms were aligned in the directions of (a) Chiba, (b) eastern Kanagawa and (c) western Tokyo. Each trace was multiplied by the hypocentral distance in order to compensate for geometrical spreading. Locations of used stations and epicentre are shown in (d).

basin were observed in waveforms recorded at TKY014 (Fig. 8b), but unclear onset and spindle-shape *S* waves were not observed. Similar coda waves were also observed at CHB014 (Fig. 8c). During events B–E, onset of *S* waves is clear, whereas unclear onset and spindle shape only appear in event A.

Spindle-shape *S* waves are observed in areas with both thick and thin sediments, and their propagation paths are passing through the LV zone at depth of 20–40 km beneath the northwestern Chiba. Thus, we concluded that the cause of the spindle-shape *S* waves with unclear onset and strong peak delay is the seismic wave scattering

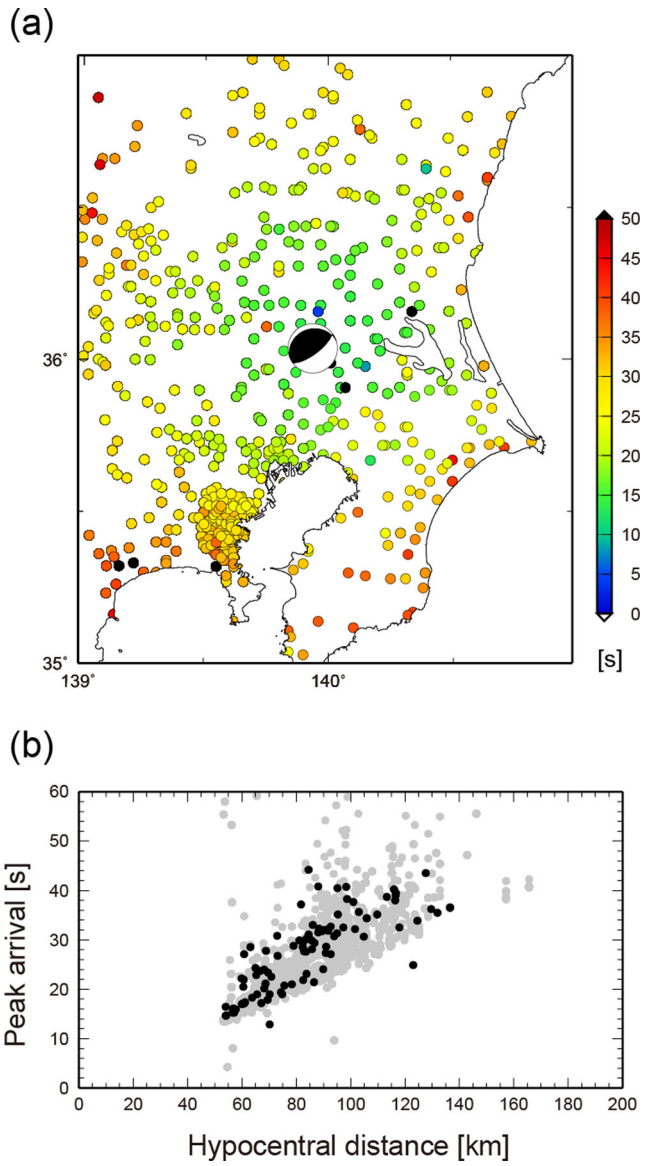

Figure 5. (a) Spatial distribution and (b) hypocentral distance change in peak arrival time of horizontal velocity motions for frequency of 2–4 Hz during the M_w 5.0 earthquake that occurred at a depth of 53 km beneath southern Ibaraki on 2005 October 16. Black circles and grey circles in (b) indicate peak arrival times for Chiba and all other regions, respectively.

due to specific heterogeneous velocity structure in the LV zone beneath northwestern Chiba. Furthermore, these features may not be attributed to scattering and trap due to shallow LV sediments in the Kanto basin.

3 2-D FDM SIMULATION OF SEISMIC WAVE PROPAGATION USING A REALISTIC LAYERED STRUCTURE

3.1 Simulation method and model

To confirm our hypothesis and to investigate heterogeneous structure beneath the northwestern Chiba, we conducted FDM simulations of seismic wave propagation using a realistic layered background velocity structure with stochastic random velocity heterogeneities. First, we conducted 2-D FDM simulations rather than the more realistic 3-D simulations. Although scattering and propagation of seismic waves are restricted to a 2-D plane, the cost of 2-D calculations is much cheaper than 3-D calculations. Therefore, we can examine many possible models through 2-D simulations. After studies based on 2-D simulations, the number of possible heterogeneous models would significantly decrease and the number of required simulations in 3-D models would also decrease.

The model of 2-D simulation covered an area of 245 km in horizontal direction and 122.5 km in depth (along profile X–X' in Fig. 9a), which was discretized by a grid interval of 0.015 km. The propagation of seismic waves was calculated by solving the equation of motion in a 2-D elastic medium based on the fourth-order staggered-grid FDM technique (Levander 1988; Graves 1996). To effectively conduct such large-scale 2-D simulations, we employed a parallel FDM simulation code based on domain partitioning procedure using large number processors through a message passing interface (Furumura & Chen 2004).

The background velocity structure was constructed using the layered structure model proposed by Koketsu *et al.* (2008), which is one of the latest and most widely used velocity structure model for the evaluation of strong and long-period ground motions for large earthquakes. We assumed a frequency-dependent Q^{-1} model for P and S waves with a central frequency of $f_0 = 2$ Hz according to the method of Robertsson (1994) (see Robertsson 1994; Hestholm 1999; Maeda *et al.* 2013 for more details). The physical parameters for velocity, density and anelastic attenuation for each layer are shown in Table 3.

We applied suitable boundary conditions for a solid-to-air interface at free surface for FDM simulation, as developed by Okamoto & Takenaka (2005). We applied this boundary condition in vertical (z) and horizontal (x) directions across solid-to-air boundaries and assumed air parameters of $V_P = 0.0$ km s^{-1}, $V_S = 0.0$ km s^{-1}, $\rho = 0.001$ g cm^{-3}.

In order to model small-scale velocity heterogeneities in the subsurface structure, we employed stochastic random velocity fluctuations characterized by a von Kármán-type power spectral density function (PSDF) in the wavenumber domain as (Klimeš 2002; Sato *et al.* 2012):

$$P(k) = \frac{4\pi\varepsilon^2 a_h a_z \kappa}{\left(1 + a_h^2 k_h^2 + a_z^2 k_z^2\right)^{\kappa+1}},$$

where ε is the rms value of the fluctuation, a_h and a_z are the correlation distances in the horizontal and vertical directions, respectively, k_h and k_z are the wavenumbers and κ is the decay rate of the PSDF at larger k. In the case of $\kappa = 0.5$, the von Kármán PSDF coincides with the exponential PSDF. Based on previous studies, detailed parameters characterizing velocity heterogeneities for each layer are shown in Table 4 (Furumura & Kennett 2005; Saito *et al.* 2005; Takemura *et al.* 2009; Takemura & Furumura 2013). In the LV sediment, we assumed stronger (i.e. smaller a and larger ε) velocity heterogeneities compared to those of the crust and upper mantle. No random velocity heterogeneity was assumed in the oceanic crusts of both subducting plates, because of a lack of information from previous studies.

The random velocity fluctuation in 2-D space $\xi(x,z)$ was first calculated in the wavenumber domain by adjusting the desired PSDF to the 2-D Fourier transform of the sequence of random numbers. The resultant fluctuation model in the wavenumber domain was transformed back to the physical domain using the inverse 2-D Fourier transform. Then, a stochastic random fluctuation in 2-D space $\xi(x,z)$ was embedded over an average background velocity $V_0(x,z)$, which

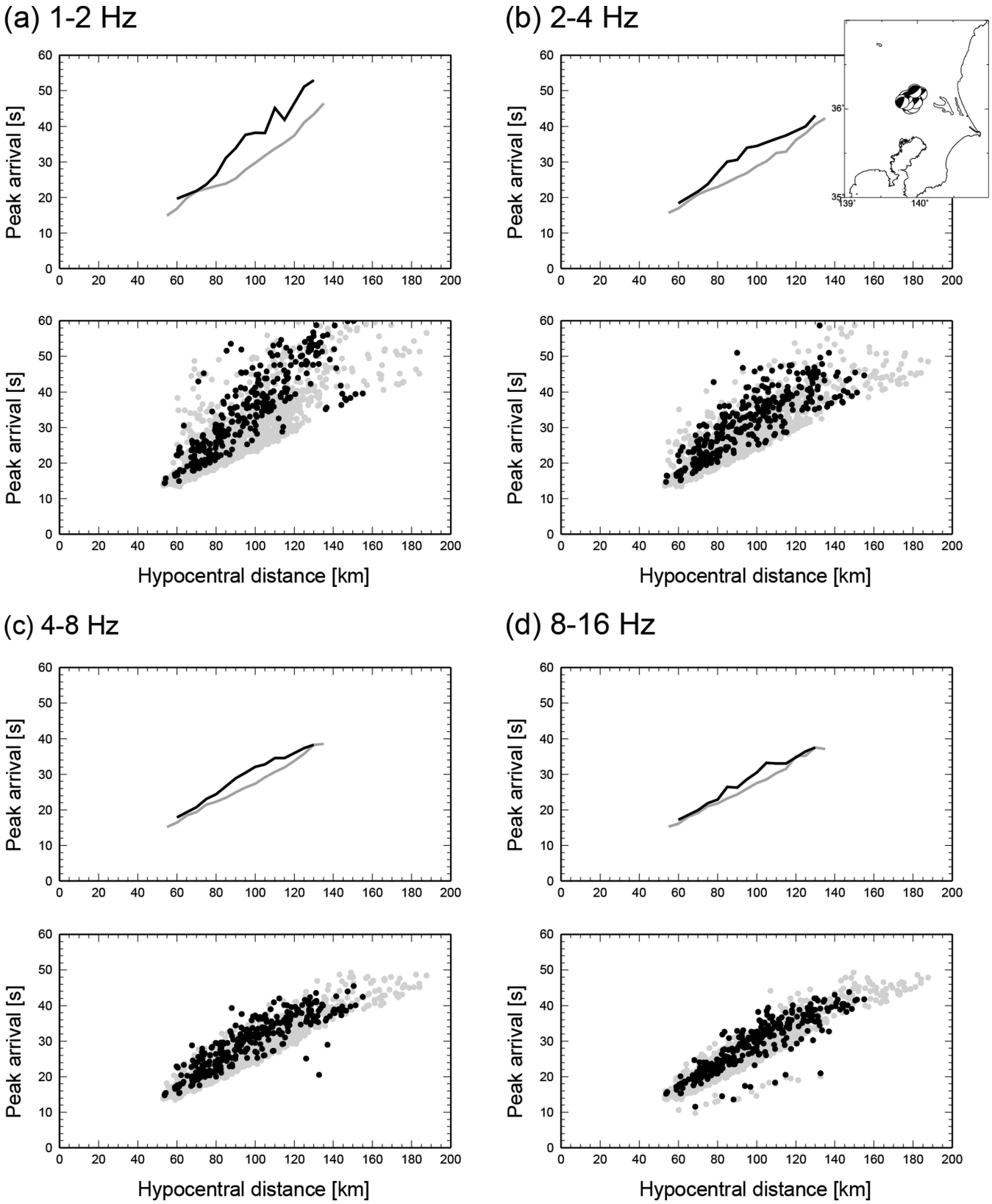

Figure 6. Peak arrival times of horizontal velocity motions as a function of hypocentral distance for each frequency band derived from 10 relatively deep earthquakes (50–60 km; see Table 1). The focal mechanisms of used events are shown in the upper right of (b). Symbols for peak arrivals are the same as those used in Fig. 5, and black and grey lines indicate the moving average curves of peak arrival times for Chiba and all other regions, respectively.

Table 1. Earthquake data used for the peak time analysis.

Origin time (local time)	Longitude	Latitude	Depth [km]	M_w
2005.02.16 04:46	139.896	36.036	53.0	5.4
2005.07.28 19:15	139.846	36.126	56.0	4.9
2005.10.16 16:05	139.937	36.039	53.0	5.0
2008.04.04 19:01	139.828	36.120	56.0	4.8
2011.03.24 08:56	140.042	36.178	53.0	4.8
2011.04.02 16:55	139.962	36.027	56.0	4.8
2011.04.26 21:12	139.976	36.086	59.0	4.9
2012.01.17 12:30	139.861	36.066	53.0	4.7
2012.02.11 10:26	139.788	36.087	59.0	4.8
2012.05.18 17:18	139.841	36.136	59.0	4.8

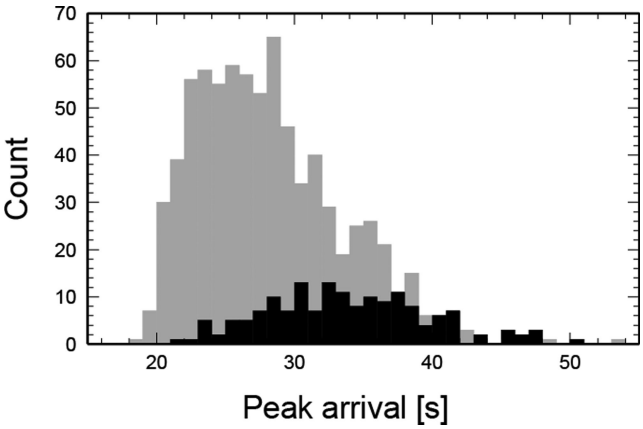

Figure 7. Histogram of the peak arrival times for frequency of 2–4 Hz at hypocentral distance of 80–120 km derived from 10 earthquakes that occurred at depths of 50–60 km beneath southern Ibaraki (see Table 1 and upper right of Fig. 6b). Black and grey bars represent the frequencies of peak arrival times for Chiba and all other regions in Kanto, respectively.

can be described as $V(x,z) = V_0(x,z)[1+\xi(x,z)]$. We assumed correlated velocities (V_P and V_S) and density ρ according to Birch's law (Birch 1961; Sato *et al.* 2012). Fig. 9(b) shows the constructed *S*-wave velocity structure model in 2-D FDM simulation. This model includes crust, mantle, two oceanic plates, thick sedimentary Kanto basin and complex surface topography. Using this model, we could examine the effect of both propagation path and site, including thick sediments just below the seismic stations.

A double-couple point source was set at a depth of 53 km (star in Fig. 9b), which radiates *P* and *SV* waves. The source time function $\dot{M}(t)$ is represented by a single-cycle Kupper wavelet according to the following equation (Mavroeidis & Papageorgiou 2003):

$$\dot{M}(t) = \frac{9\pi M_0}{16 T_0}\left[\sin\frac{\pi t}{T_0} - \frac{1}{3}\sin\frac{3\pi t}{T_0}\right] \quad \text{for } 0 \le t \le T_0,$$

where T_0 is the characteristic source duration time, and M_0 is the seismic moment. Assuming the $T_0 = 0.5$ s and $M_0 = 1.0$, the dominant frequency in this simulation was approximately 2 Hz. The focal mechanism of the seismic source with strike/dip/rake = 53/70/83° was adjusted for the 2-D simulation (*x*–*z* plane).

3.2. Results of simulation using a simple layered structure

We initially conducted 2-D FDM simulation of seismic wave propagation using a layered background velocity structure with a uniform distribution of velocity heterogeneity for each layer. Fig. 10 illustrates the snapshot sequence of seismic wave propagation at times t = 10, 15 and 30 s from the earthquake origin time. The 2-D seismic wavefield was separated into *P* (red) and *S* (green) wave contributions by calculating divergence and curl of the 2-D wavefield, respectively. Strong *S* waves radiated from the seismic source propagated through the heterogeneous oceanic plate structure, with repeated scattering, diffraction, and refraction at the velocity boundaries. In the middle and last frames (t = 15 and 30 s), strong amplification and energy trapping of *S* waves in the sedimentary layers were clearly observed (see dashed eclipse B in Fig. 10).

Fig. 11 shows normalized rms envelopes for frequency band of 2–4 Hz derived from simulation result and observation. Note that rms envelopes were calculated as the sum of the envelopes for all components and then normalized by the maximum amplitude of each trace. In order to obtain statistical properties of high-frequency seismic wavefield, we conducted FDM simulations with respect to 10 realizations of stochastic random velocity heterogeneities and then calculated the ensemble average using 10 rms envelopes at each station. Station locations are shown in the top panel of the snapshot in Fig. 10 (t = 10 s).

At shorter distances (Figs 11a and b), simulated rms envelopes well explained the observed envelope shapes. Traveltime, duration and coda excitation of *S* waves showed good agreement with observations. The amplitude and decay rate of coda waves were slightly different from the observations, because the simulation was conducted in 2-D space. As distance increases (Figs 11c and d), simulated envelopes still showed clear and impulsive *S* waves with long duration coda due to LV sediments in the Kanto basin. However, observed *S* waves showed strong peak delay and spindle shape. This discrepancy between simulation and observation at larger distances did not change even when stronger velocity heterogeneities were assumed in the sedimentary basin (results are not shown here because of the restriction of space).

3.3. Effect of small-scale velocity heterogeneity in the high V_P/V_S zone and oceanic crust

We assumed an LV zone at depth of 20–40 km beneath the northwestern part of Chiba (mark 'A' in Fig. 10). In our simulation, which used a layered structure model by Koketsu *et al.* (2008), the LV zone estimated by tomography studies corresponds to the lower crust above the subducted Philippine Sea Plate. According to the tomography study by Matsubara *et al.* (2005), we set the average *S*-wave velocity of $<V_S>$ = 3.4 km s^{-1} in the LV zone without changing V_P and ρ.

Simulation result is shown in Fig. 12. Note that rms envelopes at shorter distances did not change when the LV zone was introduced, because this zone has little relevance to the propagation path from the hypocentre to stations. Although peak arrival times at larger distances were slightly delayed compared to the simulation without LV zone, the peak delay was very weak, and observed spindle-shape *S* waves were not reproduced.

The observed strong peak delay at Chiba has dominant frequency of 1–8 Hz, and its band-limited feature may not be explained by the von Kármán PSDF usually employed in the modelling of velocity heterogeneity in the crust. In order to enhance the PSD of velocity fluctuation in the LV zone for this frequency range, we superposed a Gaussian PSDF (a = 0.5 and ε = 0.10) on the background exponential PSDF (a = 3.0 and ε = 0.07). Fig. 13 shows the PSDFs of velocity fluctuations of heterogeneities in the LV zone as a function of wavenumber k (or frequency assuming V_S = 3.40 km s^{-1} with

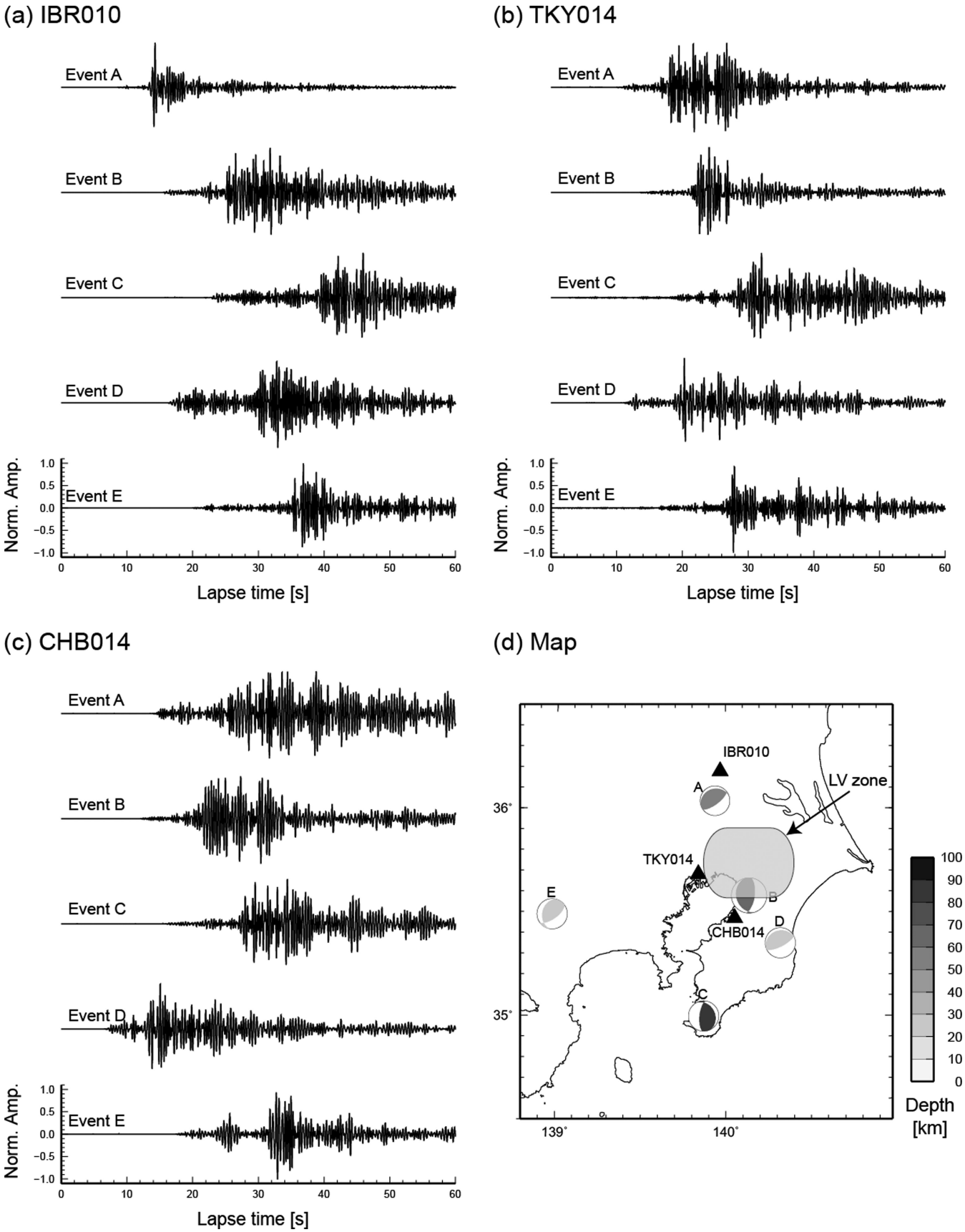

Figure 8. Filtered radial component velocity seismograms for frequency of 2–4 Hz recorded at 3 K-NET stations (a–c) during various earthquakes that occurred around the Kanto region. Each trace was normalized by its maximum amplitude. The shaded area indicates the LV zone estimated at depth of 20–40 km, as derived from tomography studies.

Table 2. Earthquake data used to create Fig. 8.

	Origin time (local time)	Longitude	Latitude	Depth [km]	M_w
A	2005.10.16 16:15	139.937	36.039	53.0	5.0
B	2005.07.23 16:34	140.138	35.582	68.0	6.0
C	2012.07.03 11:31	139.870	35.000	89.0	5.1
D	2011.12.03 05:55	140.322	35.352	20.0	5.1
E	2012.01.28 07:43	138.977	35.489	23.0	5.1

$f = V_S\, k/2\pi$). By superposing a Gaussian PSDF on an exponential PSDF, the new PSDF in frequency range of 1–8 Hz was significantly enhanced compared to the ordinary exponential PSDF. In addition, the PSDFs were not significantly different at higher frequencies (>8Hz). We also added the same velocity heterogeneities to the oceanic crust of the Philippine Sea Plate for the reasons stated below.

Fig. 14 shows a comparison between the observed and simulated rms envelopes derived from the model with LV zone and strong heterogeneities. Simulated envelopes at larger distances (Figs 14c and d) had a strong peak delay and unclear *S*-wave onset. Observed spindle-shape *S*-wave envelopes were well reproduced by introducing strong heterogeneity in the LV zone and oceanic crust of the Philippine Sea Plate.

To determine the distribution of strong velocity heterogeneities, we conducted additional 2-D FDM simulations with changing the region where strong velocity heterogeneities are assumed. Fig. 15

Table 4. Parameters characterizing the stochastic random velocity fluctuations for each layer.

	a_h [km]/a_z [km]	ε	PSDF type
Sedimentary layer	1.0/1.0	0.07	Exponential
Basement and upper crust	3.0/3.0	0.05	Exponential
Lower crust	3.0/3.0	0.07	Exponential
Mantle	10.0/10.0	0.02	Exponential
Oceanic plate	10.0/0.5	0.02	Exponential

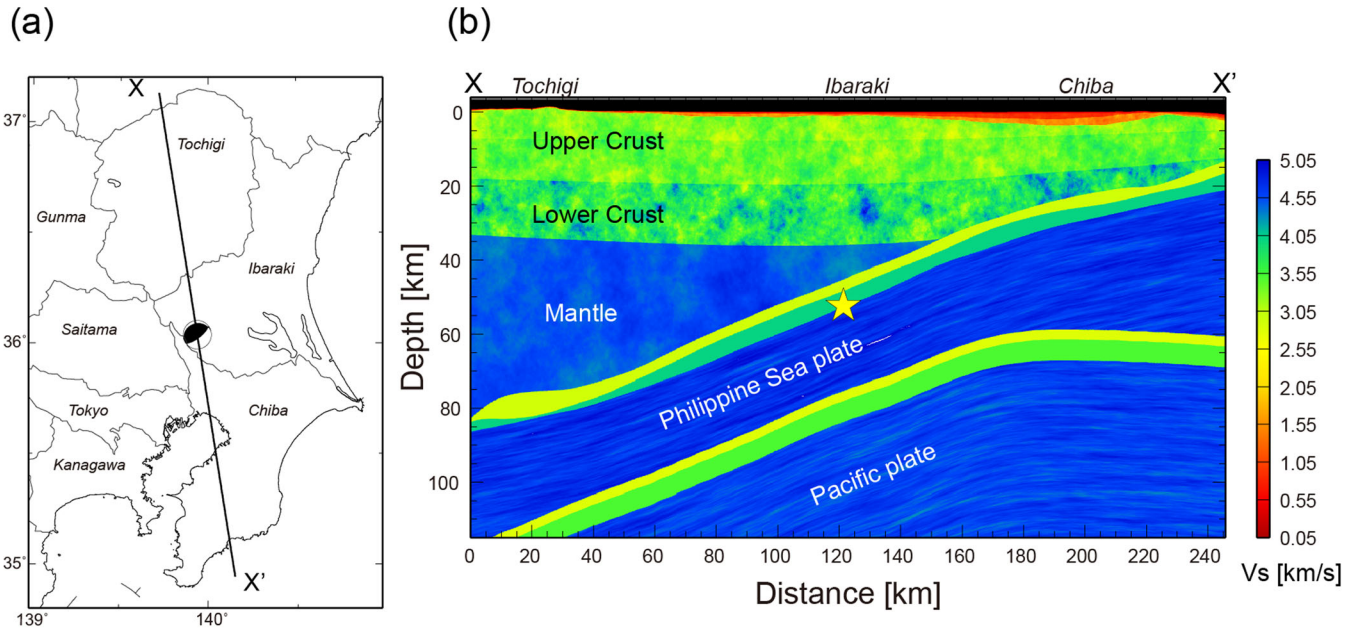

Figure 9. (a) Map of the Kanto region, and (b) the *S*-wave velocity structure in 2-D simulation model along the *X*–*X*′ profile. The focal mechanism of the event used in the 2-D simulation is shown on the map, and the star in (b) illustrates the location of seismic source.

Table 3. Physical parameters for *P*- and *S*-wave velocity, density and anelastic attenuation for each layer referred by Koketsu *et al.* (2008).

	V_P [km s^{-1}]	V_S [km s^{-1}]	ρ [g cm^{-3}]	Q_P	Q_S
Sedimentary layer 1	1.8	0.5	1.95	170	100
Sedimentary layer 2	2.3	0.9	2.10	306	180
Sedimentary layer 3	3.0	1.5	2.25	510	300
Basement	5.5	3.2	2.65	680	400
Upper crust	5.8	3.4	2.70	680	400
Lower crust	6.4	3.8	2.80	680	400
Upper mantle	7.5	4.5	3.20	850	500
Philippine Sea Plate					
Oceanic crust layer 2	5.0	2.9	2.40	340	200
Oceanic crust layer 3	6.8	4.0	2.90	510	300
Oceanic mantle	8.0	4.7	3.20	850	500
Pacific Plate					
Oceanic crust layer 2	5.4	2.8	2.6	340	200
Oceanic crust layer 3	6.5	3.5	2.8	510	300
Oceanic mantle	8.1	4.6	3.4	850	500

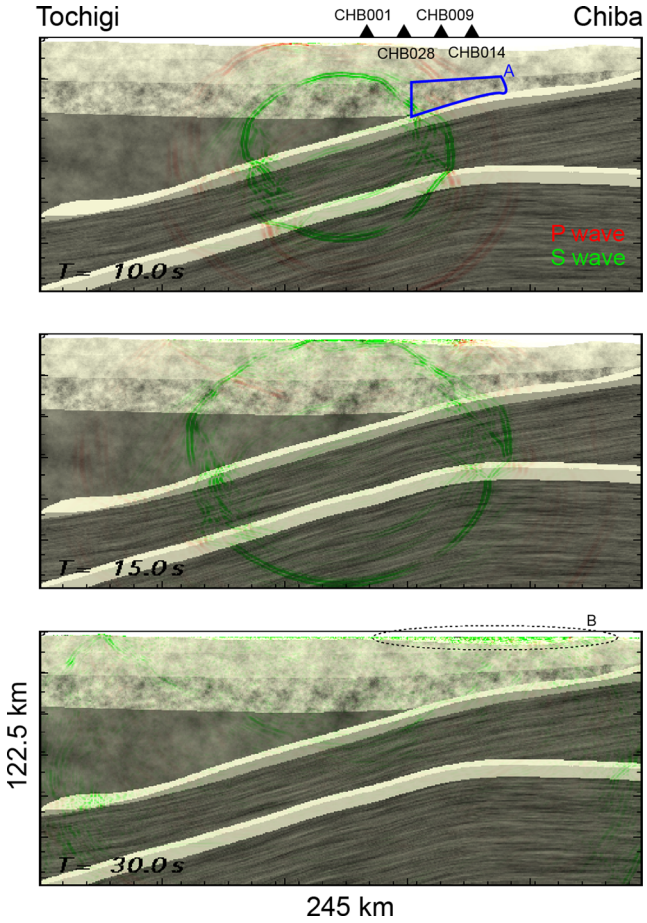

Figure 10. Snapshots of the simulated seismic velocity wavefield at $T = 10$, 15 and 30 s from earthquake origin time, showing P (red) and S (green) wave propagation. In an earlier snapshot ($T = 10$ s), locations of stations and low-velocity zone assumed in later simulations (mark A in the top panel) are also plotted.

shows the rms envelopes recorded at distance of 63 km from the epicentre (CHB014), as derived from the simulation results. The model with strong heterogeneity in the oceanic crust alone (Fig. 15a) could not reproduce observed spindle-shape S waves. In addition, peak delay was weak compared to observed envelope. By introducing strong velocity heterogeneity in the LV zone (Figs 15b and c), peak delay and large amplitude of later arrivals were clearly shown. Simulation results indicated that strong velocity heterogeneity is required in the LV zone beneath the northwestern Chiba. The model with strong velocity heterogeneity in both the LV zone and oceanic crust better explained observed spindle shape and peak delay of S waves at Chiba (Fig. 15d).

In 2-D simulations, we examined the effect of strong velocity heterogeneity characterized by the superposition of a background exponential PSDF (with $a = 3$ km, $\varepsilon = 0.07$) and a Gaussian PSDF (using only $a = 0.5$ km, $\varepsilon = 0.10$). To determine the parameters characterizing strong velocity heterogeneity in the LV zone and oceanic crust, comparison of simulation results changing correlation distances and rms values of the Gaussian PSDF is required. However, in general, 2-D simulations cannot include 3-D effects, such as seismic wave scattering, diffraction and energy traps due to the 3-D heterogeneous structure. Therefore, to examine more quantitative analysis, 3-D FDM simulations using realistic heterogeneous structure models are required.

4 SIMULATION IN A 3-D MEDIUM

4.1 Estimation of small-scale velocity heterogeneity in the LV zone

To estimate parameters characterizing strong velocity heterogeneity in the LV zone and oceanic crust of Philippine Sea Plate, we conducted 3-D FDM simulations of seismic wave propagation assuming the heterogeneous structure model discussed in the previous section.

The model of 3-D simulation covered an area of 150 km × 64 km in horizontal directions, and 75 km in vertical direction (rectangle region in Fig. 1b), which was discretized by a grid interval of 0.05 km. The parallel FDM scheme, layered background velocity structure and LV zone beneath northwestern Chiba (shown as the lower crust beneath the shaded area in Fig. 1b) were the same as those employed in 2-D simulations. A relatively coarse grid (0.05 km) was used compared to the 2-D simulation because of limitations in calculation resources (e.g. CPU power and memory size). Therefore, in the 3-D simulation, the minimum S-wave velocity in sedimentary of the Kanto basin was assumed to be 1.5 km s^{-1} and maximum frequency is 4 Hz in 3-D simulation.

To qualitatively compare simulation results with observations, we used the Centroid Moment Tensor (CMT) solution for an event that occurred at a depth of 53 km beneath southern Ibaraki on 2005 October 16 as derived by F-net. We assumed a focal mechanism with a strike/dip/rake = 53/70/83° and $M_w = 5.3$. We employed a normalized source time function, which was represented by an asymmetric cosine function according to the following equation (Ji *et al.* 2003):

$$\dot{M}(t) = \begin{cases} \frac{1}{t_s+t_e}\left[1-\cos\left(\frac{\pi t}{t_s}\right)\right], \text{if } 0 < t < t_s \\ \frac{1}{t_s+t_e}\left[1-\cos\left(\frac{\pi(1-t)}{t_s}\right)\right], \text{if } t_s < t < t_s + t_e \\ 0, \text{if } t_s + t_e < t \end{cases},$$

where t_s is the starting rise time, t_e is the ending rise time and $t_s + t_e$ is the total pulse duration. Because two parameters (t_s and t_e) control rise time and duration for the source rupture process, this function is more realistic compared to the single-cycle Kupper wavelet in the 2-D simulation. We set $t_s = 0.125$ and $t_e = 0.125$, which were determined from the observed S-wave spectrum at F-net stations.

Stochastic random velocity heterogeneity models were characterized by same parameters as those used in the 2-D simulations (Table 4). In addition, we embedded strong velocity heterogeneities in the LV zone and oceanic crust that might be cause of observed spindle-shape S waves at Chiba. Strong velocity heterogeneity was constructed by superposition of a Gaussian PSDF and a background exponential PSDF ($a = 3$ km, $\varepsilon = 0.07$). We assumed a set of parameters for the Gaussian PSDF with correlation distances ($a = 0.5$, 1 and 2 km) and rms values of fluctuation ($\varepsilon = 0.05$, 0.07 and 0.09). We also conducted a FDM simulation in the 3-D model without considering strong velocity heterogeneity in the LV zone and oceanic crust (hereafter called the 'initial model').

To determine the preferable parameters from various heterogeneous models, we calculated residual values from observed peak arrival times using the following equation:

$$\text{residual} = \frac{1}{N}\left|\sum_i \left[T_P^{\text{Cal}}(D_i) - T_P^{\text{Obs}}(D_i)\right]\right|,$$

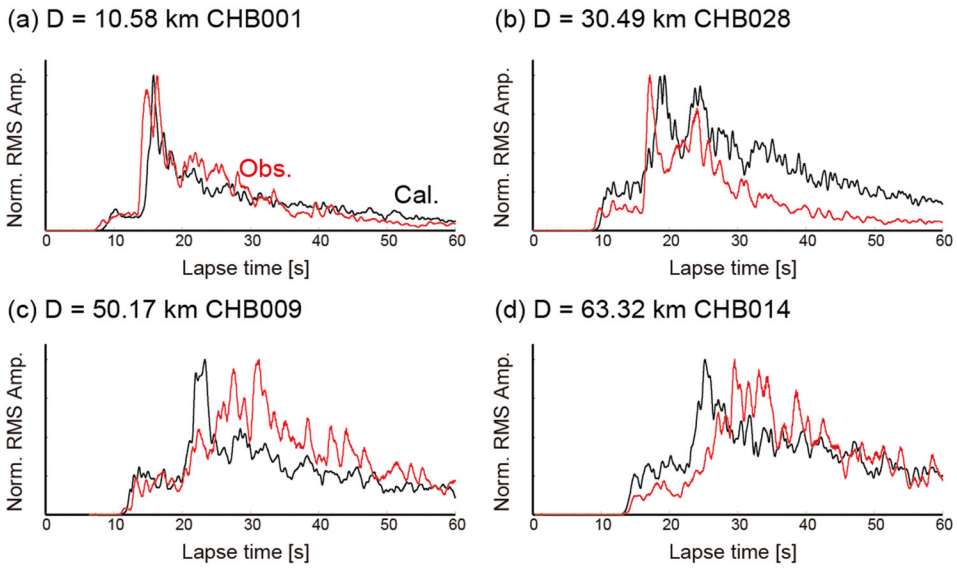

Figure 11. Comparison of normalized rms envelopes derived from observation (red lines) and simulation (black lines) for the layered structure model with stochastic random velocity heterogeneities.

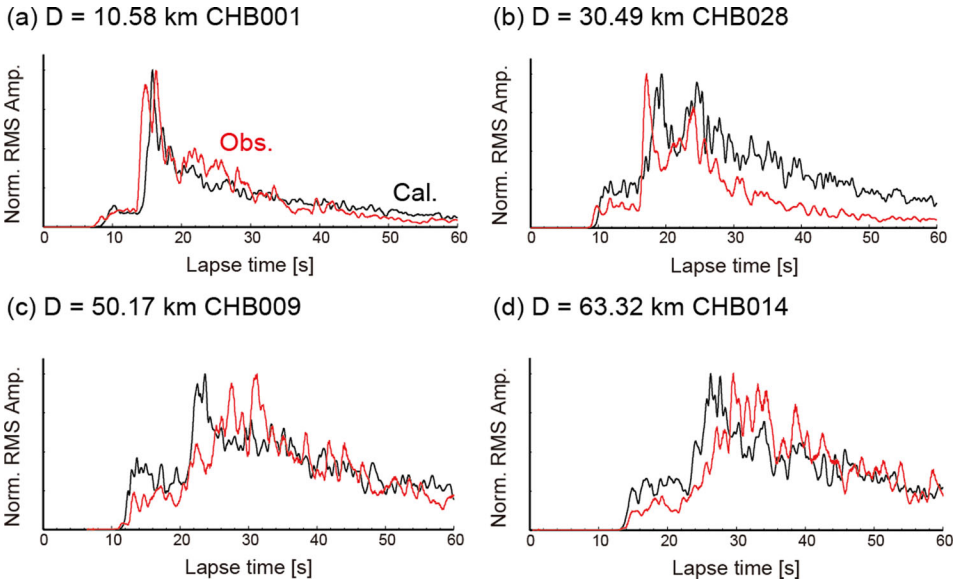

Figure 12. Comparison of normalized rms envelopes derived from observation (red lines) and simulation (black lines) for the model with an LV zone.

where T_P^{Cal} and T_P^{Obs} are the peak arrival times derived from simulation and observation, D_i is the hypocentral distance to the ith station and N is the total number of simulated peak arrival time data. Simulated peak arrival times were measured using two horizontal seismograms recorded at virtual seismic stations that were uniformly distributed at intervals of 5 km in the calculation region. Calculated residual values were normalized by the residual value of the initial model.

Tables 5 and 6 show the residual values for each model normalized by the residual of the initial model. By introducing strong velocity heterogeneities in the LV zone and oceanic crust of the Philippine Sea Plate, normalized residual values decreased compared to those of the initial model (residual = 1.0). The most preferable models for frequencies of 1–2 and 2–4 Hz were the velocity heterogeneities characterized by the Gaussian PSDF with $a = 2$ km, $\varepsilon = 0.09$ and $a = 1$ km, $\varepsilon = 0.07$ superposed on the background exponential PSDF with $a = 3$ km, $\varepsilon = 0.07$.

We concluded that the cause of strong peak delay and spindle-shape S waves at Chiba is strong seismic wave scattering due to strong velocity heterogeneities localized in the LV zone and oceanic crust of the Philippine Sea Plate. Localized strong velocity heterogeneities are characterized by the Gaussian PSDF with $a = 1$–2 km and $\varepsilon = 0.07$–0.09 superposed on the background exponential PSDF with $a = 3$ km and $\varepsilon = 0.07$.

Fig. 16 shows a comparison between observed and simulated peak arrival times for frequencies of 1–2 Hz (Figs 16a and b) and 2–4 Hz (Figs 16c and d). The initial model showed earlier peak arrival times for both frequency bands compared to observations

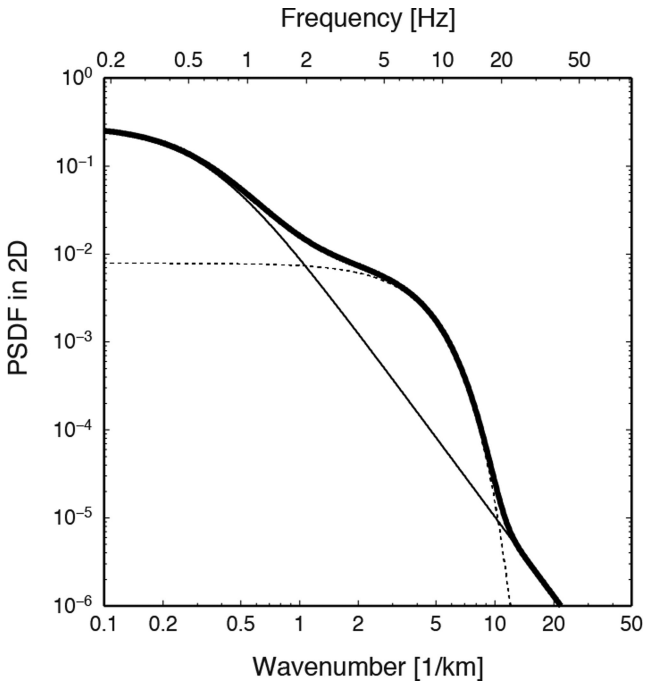

Figure 13. Assumed PSDF of stochastic random velocity heterogeneity in the LV zone as a function of wavenumber (or frequency assuming $V_S = 3.40\,\mathrm{km\ s^{-1}}$ with $f = V_S\ k/2\pi$). Solid and dotted lines are exponential ($a = 3$ km and $\varepsilon = 0.07$) used in previous simulations, and Gaussian ($a = 0.5$ km and $\varepsilon = 0.10$) PSDF, respectively. The bold line is the result of the enhanced model constructed by the superposition of exponential and Gaussian PSDFs.

(Figs 16a and c). By introducing preferable strong velocity heterogeneities (Figs 16b and d), peak arrival times were delayed at distances over 60–70 km, and observed features were well explained.

At frequencies of 1–2 and 2–4 Hz, the wavelengths of S waves propagating through the LV zone ($V_S = 3.4\,\mathrm{km\ s^{-1}}$) were 2.26 and 1.13 km, respectively, which corresponded to correlation distances ($a = 1$–2 km) for the preferable Gaussian PSDF for each frequency band. Strong seismic scattering occurred in the LV zone due to the velocity heterogeneity with a characteristic scale that was comparable to the wavelength of S waves.

4.2 Effect of strong velocity heterogeneity in the LV zone

We determined the velocity heterogeneity in the LV zone and oceanic crust of the Philippine Sea Plate by comparing simulated and observed peak arrival times. To investigate the effect of strong velocity heterogeneity in the LV zone on high-frequency seismic wave propagation, we then compared simulation result for the most preferable model with observation. Fig. 17 shows velocity seismograms of radial components derived from the model without/with strong velocity heterogeneities (superposition of background exponential PSDF with $a = 3$ km, $\varepsilon = 0.07$ and Gaussian PSDF with $a = 1$ km, $\varepsilon = 0.07$) and from observation. Station locations were the same as those shown in Fig. 4(a), and amplitude of each trace was normalized by its maximum amplitude. The results of simulation without strong heterogeneity showed long-duration and distorted S waves associated with the LV sediments in the Kanto basin at epicentral distances larger than 50 km, but a sudden change in S-wave shape and peak arrival time did not appear. In contrast, the simulated seismograms derived from the model with strong velocity heterogeneity (Fig. 17b) showed spindle-shape S waves with strong peak delay that agreed with observation (Fig. 17c). The sudden change in peak arrival time and envelope shape at 40 km from the epicentre was well reproduced.

Fig. 18 shows the distributions of peak ground velocity (PGV) for frequency band of 2–4 Hz, as derived from simulations with/without strong velocity heterogeneities. In our simulations, we did not take into account the effect of site amplification due to LV ($V_S < 1.5\,\mathrm{km\ s^{-1}}$) layers, because of the cost of 3-D simulations. Therefore, we could not directly compare PGV values between our simulations and observation. PGV values derived from the model without strong velocity heterogeneities gradually decayed with increasing distance.

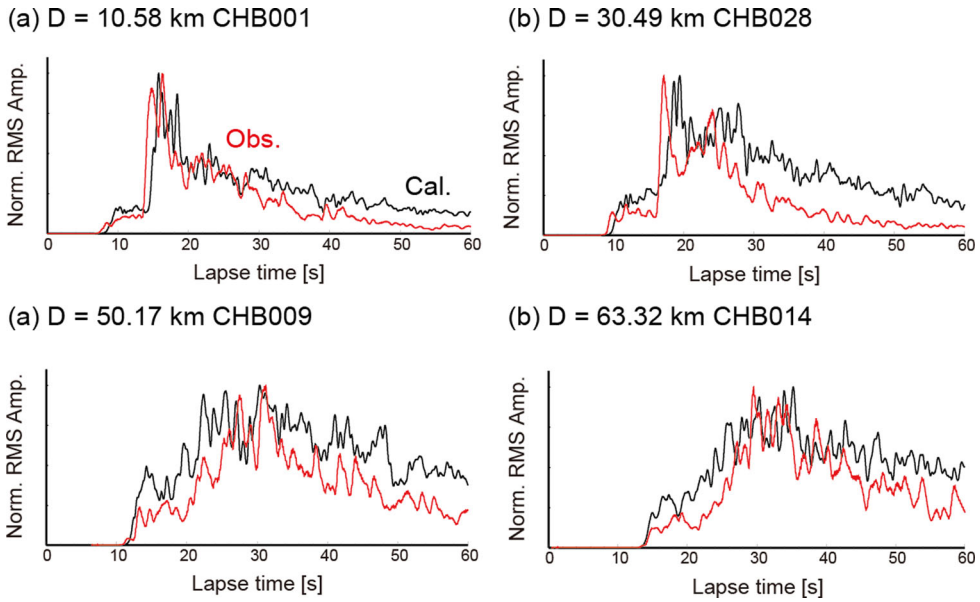

Figure 14. Comparison of normalized rms envelopes derived from observation (red lines) and simulation (black lines) for the model including strong velocity heterogeneity into the LV zone and the oceanic crust of the Philippine Sea Plate.

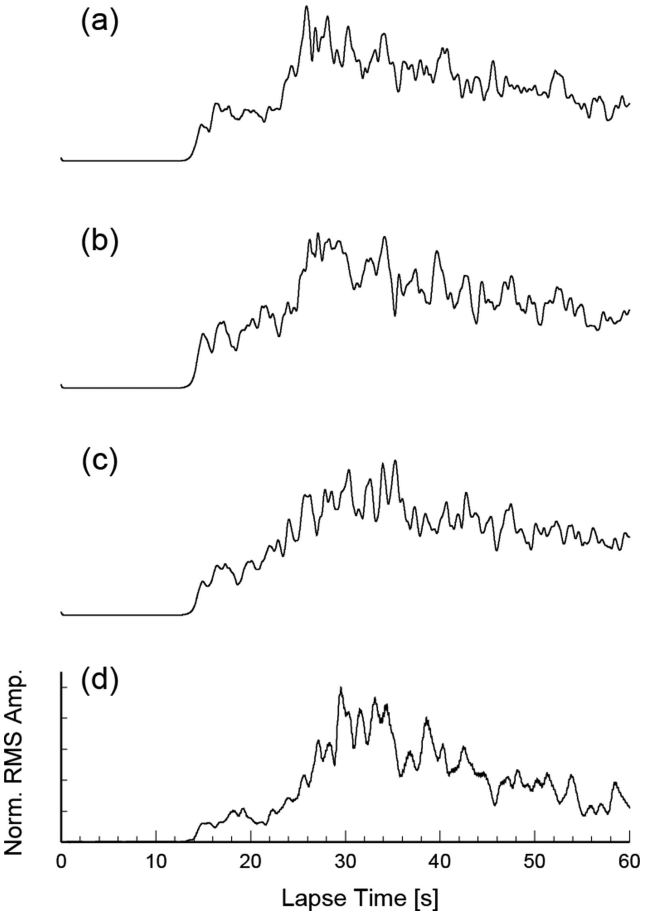

Figure 15. Comparison between simulated and observed rms envelopes at station CHB014. Simulation results included strong heterogeneities in (a) the oceanic crust of the Philippine Sea Plate alone, (b) in the LV zone alone, (c) in both the LV zone and the oceanic crust of the Philippine Sea Plate and (d) observation.

Table 5. Normalized residual values for frequency of 1–2 Hz derived from simulation results in each model.

	$\varepsilon = 0.05$	0.07	0.09
$a = 0.5$ km	0.927	0.801	0.628
$a = 1.0$ km	0.809	0.750	0.427
$a = 2.0$ km	0.771	0.671	0.348

By introducing strong velocity heterogeneities, PGV values suddenly dropped at the northwestern Chiba, and weaker PGV values appeared at the central and southern parts of Chiba. Our simulation results reproduced the observed PGV decay at the northwestern Chiba (Fig. 18c).

Table 6. Normalized residual values for frequency of 2–4 Hz derived from simulation results in each model.

	$\varepsilon = 0.05$	0.07	0.09
$a = 0.5$ km	0.627	0.187	0.521
$a = 1.0$ km	0.441	0.0999	0.811
$a = 2.0$ km	0.850	0.276	0.802

5 DISCUSSION AND CONCLUSION

Using the dense strong motion networks (i.e. K-NET/KiK-net and SK-net) in the Kanto region, we analysed the seismograms of local earthquakes. For ray paths that passed through the LV zone at depth of 20–40 km beneath northwestern Chiba, significant changes in the shapes and peak arrival times of *S* waves for frequency of 1–8 Hz were observed at the central and southern Chiba. Through 2-D and 3-D FDM simulations, we interpreted these observations as indicating that the strong seismic wave scattering occurred in the LV zone and then spindle-shape *S* waves were constructed. The cause of the LV zone with a high V_P/V_S ratio above the oceanic crust of the Philippine Sea Plate is interpreted as dehydration from the subducting oceanic crust (e.g. Matsubara *et al.* 2005). If the LV zone is rich in fluid supplied by the dehydration of subducting oceanic crust, strong small-scale velocity heterogeneities in the LV zone may be related to the random distribution of fluid in this volume. According to peak delay analysis of *S*-wave seismograms for microearthquakes, Takahashi *et al.* (2009) estimated strong small-scale velocity heterogeneities beneath the Quaternary volcanoes in the northeastern Japan, which are also LV zones with high V_P/V_S ratios associated with dykes and the melt of ascending magma. These similar observations obtained under different geophysical circumstances may imply that the LV zone detected from seismic tomography at depth of several tens of kilometres is essentially rich in fluid, resulting in a high scattering potential for high-frequency seismic waves.

Through FDM simulations of seismic wave propagation using a realistic 3-D structure, we demonstrated that the strong velocity heterogeneities characterized by a Gaussian PSDF ($a = 1$–2 km, $\varepsilon = 0.07$–0.09) superposed on a background exponential PSDF ($a = 3$ km, $\varepsilon = 0.07$) that are localized in the LV zone and oceanic crust can cause strong seismic wave scattering. Simulation result with such strong heterogeneities well explained the observed spindle-shape *S* waves with strong peak delay recorded at the central and southern parts of Chiba. In addition, simulation results also reproduced weaker PGV distributions observed at Chiba due to strong scattering loss in the LV zone. A similar heterogeneous model was proposed by Yoshimoto & Okada (2009) for the lithosphere beneath the southeastern Kanto region. In their study, they analysed large number of borehole seismograms on the basis of the multiple-lapse time window analysis and suggested that small-scale velocity heterogeneities, characterized by a Gaussian PSDF with $a = 1$ km and $\varepsilon = 0.10$, are required to explain estimated scattering attenuation of *S* waves. The coincidence of estimated velocity heterogeneities in two studies may indicate that their estimation might be strongly affected by the scattering due to strong velocity heterogeneities in the LV zone discussed in this study.

Attenuation features have also been studied in this region using tomographic inversion and numerical simulation (e.g. Nakamura *et al.* 2006; Furumura & Takeuchi 2007). To compare the Q values estimated in previous studies, we calculated theoretical scattering loss based on the first-order Born approximation (Sato *et al.* 2012, Chapters 4 and 5), assuming the estimated strong velocity heterogeneities (superposition of an exponential PSDF with $a = 3$ km, $\varepsilon = 0.07$ and a Gaussian PSDF with $a = 1$ km, $\varepsilon = 0.07$). Fig. 19 shows the assumed intrinsic attenuation $1/Q_{\rm Int}$ and theoretical scattering loss $1/Q_{\rm Scat}$ as a function of frequency. We also calculated the total attenuation ($1/Q_{\rm tot} = 1/Q_{\rm Int} + 1/Q_{\rm Scat}$) (plotted in Fig. 19). The expected *S*-wave attenuation was very strong in frequency range of 1–4 Hz. Our expected values strongly agreed with the Q values estimated by Nakamura *et al.* (2006) from attenuation tomography. In our simulation, intrinsic attenuation $1/Q_{\rm Int}$ was the average value

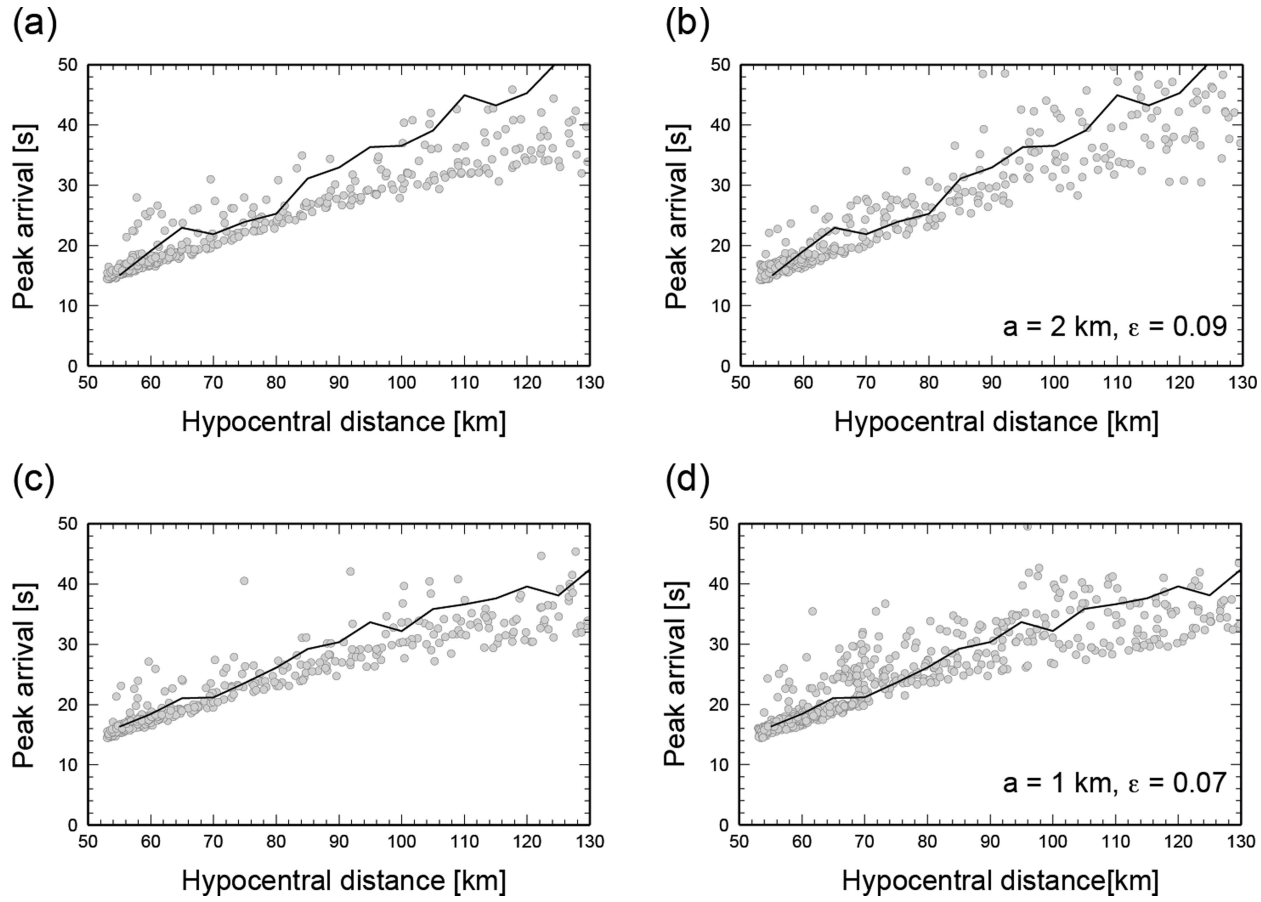

Figure 16. Comparison between observed and simulated peak arrival times in the 3-D heterogeneous model. Simulation results in (a) the model without strong Gaussian velocity heterogeneity, (b) the model with the most preferable Gaussian velocity heterogeneity for frequency of 1–2 Hz, (c) the model without strong Gaussian velocity heterogeneity and (d) the model with the most preferable Gaussian velocity heterogeneity for frequency of 2–4 Hz. Parameters of Gaussian velocity heterogeneity are shown in the lower right parts of (b) and (d). Each dot represents the value of the peak arrival time derived from simulation results. Solid lines indicate the moving average curves of observed peak arrival times at Chiba.

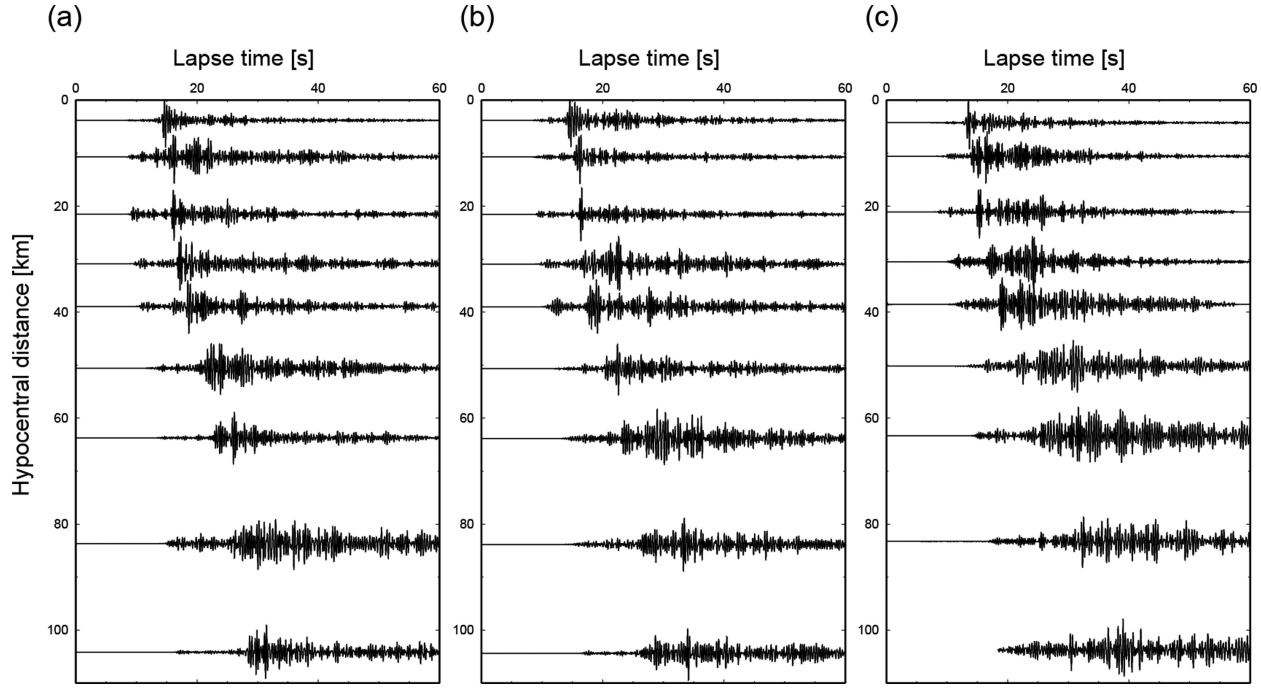

Figure 17. Comparison between simulated and observed velocity seismograms of radial component for frequency of 2–4 Hz. Simulation results were derived from (a) the model without strong Gaussian heterogeneity, (b) the model with the most preferable small-scale heterogeneity model and (c) observation. Station distribution is the same as in Fig. 4(a).

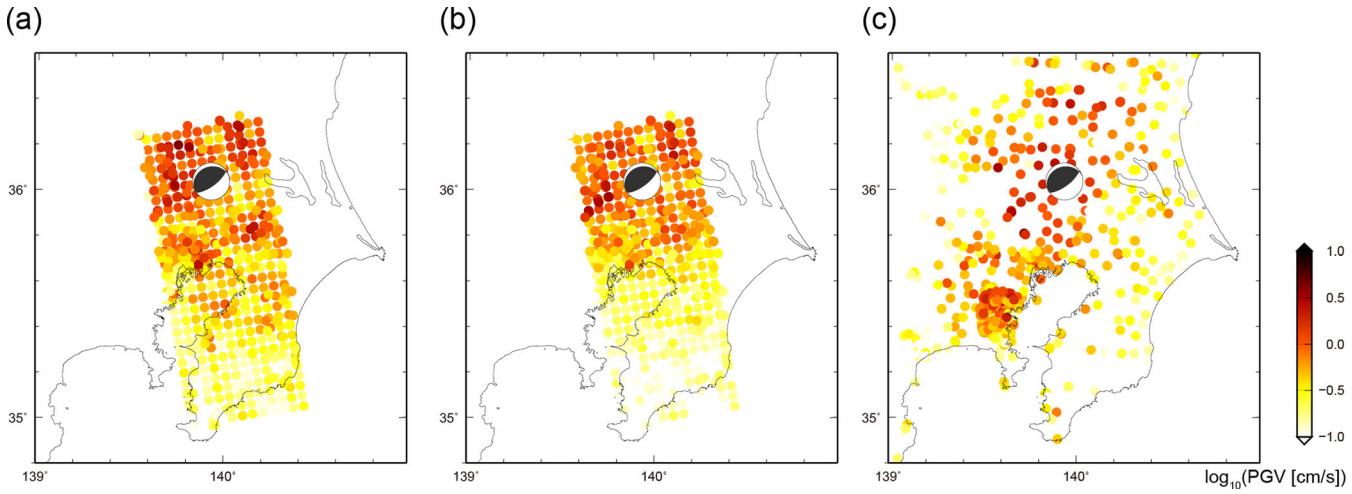

Figure 18. Comparison of the PGV distributions between simulations and observation. Simulation results were derived from (a) the model without strong Gaussian heterogeneity, (b) the model with the most preferable small-scale heterogeneity model for frequency of 2–4 Hz and (c) observation.

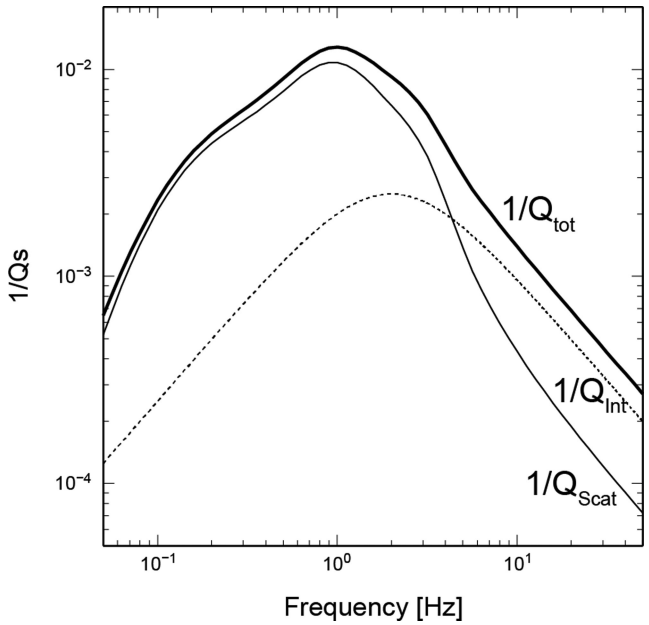

Figure 19. Assumed *S*-wave Q model in the LV zone above the Philippine Sea Plate as a function of frequency. Solid, dashed and bold lines denote intrinsic attenuation ($1/Q_{\rm Int}$) assumed in the 3-D simulation, scattering attenuation ($1/Q_{\rm Scat}$) for the estimated heterogeneous model (i.e. with a superposition of the exponential PSDF with $a = 3$ km, $\varepsilon = 0.07$ and the Gaussian PSDF with $a = 1$ km, $\varepsilon = 0.07$) and total attenuation ($1/Q_{\rm tot} = 1/Q_{\rm Int} + 1/Q_{\rm Scat}$), respectively.

of attenuation in the crust. Therefore, the observed attenuation in the LV zone could mainly be caused by seismic wave scattering due to strong velocity heterogeneity localized in this volume. Since the maximum frequency was $f = 4$ Hz in our simulation, we could not completely reproduce the band-limited features of observed distinct spindle-shape *S* waves with strong peak delay, in our simulations. However, predicted attenuation based on our estimated velocity heterogeneities had strong band-limited features.

This study focused on the LV zone beneath northwestern Chiba, but tomography studies also detected an LV zone at depth of 20–30 km beneath central Tokyo (Kamiya & Kobayashi 2000; Matsubara *et al.* 2005). Therefore, the pulse broadening of *S* waves in the direction of the southwestern part of Tokyo (Fig. 4c) could be caused by seismic wave scattering due to strong velocity heterogeneities localized in the LV zone beneath central Tokyo. This LV zone is also interpreted as dehydration from the subducting oceanic crust, but it has slightly different features compared to the LV zone beneath northwestern Chiba (as reported by Matsubara *et al.* 2005). The existence of different *S*-wave characteristics in western Tokyo and Kanagawa would therefore be expected. In future studies, a more detailed analysis using dense seismic networks, such as Hi-net, K-NET/KiK-net and SK-net, could reveal the detailed spatial distribution of fluid.

ACKNOWLEDGEMENTS

We would like to thank two anonymous reviewers and the editor, Dr. E. Fukuyama, for constructive comments that improved an earlier draft of this manuscript. We acknowledge the National Research Institute for Earth Science and Disaster Prevention, Japan (NIED) for providing the K-NET/KiK-net waveform data. SK-net waveform data were provided by the Earthquake Research Institute, University of Tokyo. The computations were conducted on the Earth Simulator at the Japan Agency for Marine-Earth Science and Technology Center (JAMSTEC) under the support of the joint research project 'Seismic wave propagation and strong ground motion in 3-D heterogeneous structure' conducted by the Earthquake Research Institute, University of Tokyo and the Earth Simulator Center. One of authors, ST, is grateful for the financial support provided from the Grant-in-Aid for JSPS (the Japan Society for Promotion of Science; No. 24.5704) fellows. Almost all the figures in this study were drawn using the Generic Mapping Tools (GMT) software package developed by Wessel and Smith (1998).

REFERENCES

Birch, A.F., 1961. The velocity of compressional waves in rocks to 10 kilobars, part 2, *J. geophys. Res.,* **66,** 2199–2224.

Fukao, Y., Hori, S. & Ukawa, M., 1983. A seismological constraint on the depth of basalt-eclogite transition in a subducting oceanic crust, *Nature,* **303,** 413–415.

Furumura, T. & Chen, L., 2004. Large scale parallel simulation and visualization of 3-D seismic wavefield using Earth simulator, *Comput. Model. Eng. Sci.,* **6,** 153–168.

Furumura, T. & Kennett, B.L.N., 2005. Subduction zone guided waves and the heterogeneity structure of the subducted plate: intensity anomalies in northern Japan, *J. geophys. Res,* **110,** B10302, doi: 10.1029/2004JB003486.

Furumura, T. & Takeuchi, H., 2007. Large earthquakes occurring beneath Tokyo metropolitan area and strong ground motion: Ansei Edo earthquake and Meiji Tokyo earthquake, *J. Geogr.,* **116,** 431–450 (in Japanese with English abstract).

Graves, R.W., 1996. Simulating seismic wave propagation in 3D elastic media using staggered-grid finite differences, *Bull. seism. Soc. Am.,* **86,** 1091–1106.

Hestholm, S., 1999. Three-dimensional finite difference viscoelastic wave modeling including surface topography, *Geophys. J. Int.,* **139,** 852–878.

Hori, S., Inoue, H., Fukao, Y. & Ukawa, M., 1985. Seismic detection of the untransformed 'basaltic' oceanic crust subducting into the mantle, *Geophys. J. R. astr. Soc.,* **83,** 169–197.

Ji., C., Helmberger, D.V., Wald, D.J. & Ma, K.F., 2003. Slip distribution and dynamic implication of the 1999 Chi-Chi, Taiwan earthquake, *J. geophys. Res.,* **108,** 2412, doi:10.1029/2002JB001764.

Kamiya, S. & Kobayashi, Y., 2000. Seismological evidence for the existence of serpentinized wedge mantle, *Geophys. Res. Lett.,* **27,** 819–822.

Kennett, B.L.N. & Furumura, T., 2001. Regional phases in continental and oceanic environments, *Geophs, J. Int.,* **146,** 562–568.

Kennett, B.L.N. & Furumara, T., 2008. Stochastic waveguide in the lithosphere: Indonesian subduction zone to Australian craton, *Geophys. J. Int.,* **172,** 363–382.

Klimeš, L., 2002. Correlation functions of random media, *Pure appl. Geophys.,* **159,** 1811–1831.

Koketsu, K. & Miyake, H., 2008. A seismological overview of long-period ground motion, *J. Seismol.,* **12,** 133–143.

Koketsu, K., Miyake, H., Fujiwara, H. & Hashimoto, T., 2008. Progress towards a Japan integrated velocity structure model and long-period ground motion hazard map, in *Proceedings of the 14th World Conference on Earthquake Engineering,* S10–038.

Levander, A.R., 1988. Fourth-order finite-difference P-SV seismograms, *Geophysics,* **53,** 1425–1436.

Maeda, T., Furumara, T., Noguschi, S., Takemura, S., Sakai, S., Shinohara, M., Iwai, K. & Lee, S.J., 2013. Seismic- and tsunami-wave propagation of the 2011 Off the Pacific Coast of Tohoku Earthquake as inferred from the tsunami-coupled finite-difference simulation, *Bull. seism. Soc. Am.,* **103,** 1456–1472.

Matsubara, M., Hayashi, H., Obara, K. & Kasahara, K., 2005. Low-velocity oceanic crust at the top of Philippine Sea and Pacific plates beneath the Kanto region, central Japan, imaged by seismic tomography, *J. geophys. Res.,* **110,** B12304, doi:10.1029/2005JB003673.

Matsubara, M., Obara, K. & Kasahara, K., 2008. Three-dimensional *P*- and *S*-wave velocity structures beneath the Japan Islands obtained by high-density seismic station by seismic tomography, *Tectonophysics,* **454,** 86–103.

Mavroeidis, G.P. & Papageorgiou, A.S., 2003. A mathematical representation of near-field ground motions, *Bull. seism. Soc. Am.,* **93,** 1099–1131.

Nakamura, R., Satake, K., Toda, S., Uetake, T. & Kamiya, S., 2006. Three-dimensional attenuation (Q_S) structure beneath the Kanto district, Japan, as inferred from strong motion records, *Geophys. Res. Lett.,* **33,** L21304, doi:10.1029/2006GL027352.

Obara, K. & Sato, H., 1995. Regional differences of random inhomogeneities around the volcanic front in the Kanto-Tokai area, Japan, revealed from the broadening of S wave seismogram envelopes, *J. geophys. Res.,* **110,** 2103–2121.

Okamoto, T. & Takenaka, H., 2005. Fluid-solid boundary implementation in the velocity-stress finite-difference method, *Zisin,* **57,** 355–364 (in Japanese with English abstract).

Robertsson, J., 1994. Viscoelastic finite-difference modeling, *Geophysics,* **59,** 1444–1456.

Saito, T., Sato, H., Ohtake, M. & Obara, K., 2005. Unified explanation of envelope broadening and maximum-amplitude decay of high-frequency seismograms based on the envelope simulation using the Markov approximation: forearc side of the volcanic front in northeastern Honshu, Japan, *J. geophys. Res.,* **110,** B01304, doi:10.1029/2004JB003225.

Sato, H., 1989. Broadening of seismogram envelopes in the randomly inhomogeneous lithosphere based on the parabolic approximation: southeastern Honshu, Japan, *J. geophys. Res.,* **94,** 17 735–17 747.

Sato, H., Fehler, M. & Maeda, T., 2012. *Seismic Wave Propagation and Scattering in the Heterogeneous Earth Structure,* 2nd edn, Springer-Verlag.

Takahashi, T., Sato, H., Nishimura, T. & Obara, K., 2007. Strong inhomogeneity beneath Quaternary volcanoes revealed from the peak delay analysis of S-wave seismograms of microearthquakes in northeastern Japan, *Geophys. J. Int.,* **168,** 90–99.

Takahashi, T., Sato, H., Nishimura, T. & Obara, K., 2009. Tomographic inversion of the peak delay times to reveal random velocity fluctuations in the lithosphere: method and application to northeastern Japan, *Geophys. J. Int.,* **178,** 1437–1455.

Takemura, S. & Furumura, T., 2013. Scattering of high-frequency *P* wavefield derived from by dense Hi-net array observations in Japan and computer simulations of seismic wave propagations, *Geophys. J. Int.,* **193,** 421–436.

Takemura, S., Furumura, T. & Saito, T., 2009. Distortion of the apparent *S*-wave radiation pattern in the high-frequency wavefield: Tottori-ken Seibu, Japan, earthquake of 2000, *Geophys. J. Int.,* **178,** 950–961.

Wessel, P. & Smith, W.H.F., 1998. New improved version of generic mapping tools released, *EOS, Trans. Am. geophys. Un.,* **79,** 579.

Yoshimoto, K. & Okada, M., 2009. Frequency-dependence attenuation of S-waves in Kanto region, Japan, *Earth Planets Space,* **61,** 1067–1075.